

Coherent and Non-Coherent Change Detection for Through the Wall Sensing of Moving Targets

Anthony Martone, Calvin Le, and Kenneth Ranney
Army Research Laboratory, 2800 Powder Mill Rd
Adelphi, MD 20783 USA

Abstract— In this paper a novel change detection technique is introduced and used to process modeling and measurement data of a person walking inside a building. The proposed change detection technique is based on non-coherent change detection. The MT signature, back-wall shadow, front-wall response, and sidelobe-artifact suppression generated by the proposed algorithm are analyzed and compared with those generated by coherent change detection. It will be shown that the proposed algorithm greatly attenuates imaging artifacts while preserving the MT signature.

I. INTRODUCTION

The detection of moving personnel inside building structures has a wide range of applications including urban military operations and search-and-rescue missions. To identify moving personnel inside buildings, a time-domain approach is considered that utilizes a low-frequency, ultra-wideband (UWB) radar. The time-domain approach to moving target indication (MTI) is considered as an alternative to a frequency-domain approach, i.e. Doppler processing, since a very small Doppler shift in backscattered frequency is generated due to: 1) the slow motion of the mover; and 2) the low frequency needed to penetrate through the wall [1].

The time domain approach is based on the change detection paradigm which is inherently similar to clutter cancellation [2]. The change detection paradigm in this paper considers a sequence of focused images generated by a stationary radar for a region of interest (ROI) inside a building. The stationary objects in the ROI remain in the same position/location in each image; however, moving personnel are at different locations. The moving personnel are detected by subtracting the focused images, thereby eliminating the stationary objects and identifying the moving target (MT) signature. The effectiveness of this time domain approach has been demonstrated for people walking inside wood and cinderblock buildings [3].

An analysis of the MT signature was conducted in previous research to determine false alarm and detection rates of 4 operational scenarios of personnel walking inside wood and cinderblock buildings [4]. Constant false alarm rate (CFAR) and morphological processing were used in addition to change detection. Our results indicated a high probability of detection (Pd) and low probability of false alarm (Pfa) for moving targets inside the wood building. However, a high Pfa was identified for moving targets inside the cinderblock building. The high Pfa is due to: a) the back-scatter from the

front-wall; b) the back-wall “shadow;” and c) sidelobe imaging artifacts. Past simulations have indicated that the “shadow” is an anticipated phenomenon due to objects blocking part of the back wall from illumination.

In this paper a novel change detection technique is introduced and used to process modeling and measurement data of a person walking inside a building. The proposed change detection technique is based on non-coherent change detection. The MT signature, back-wall shadow, front-wall response, and sidelobe-artifacts suppression generated by the proposed algorithm are analyzed and compared with those generated by coherent change detection. It will be shown that the proposed algorithm greatly attenuates imaging artifacts that lead to false alarms while preserving the MT signature.

II. FUNDAMENTALS OF COHERENT AND NON-COHERENT CHANGE DETECTION

In this section we describe the fundamentals associated with coherent and non-coherent change detection. First define $I(x, y)$ as the focused image for a region of interest, where “x” and “y” are down-range and cross-range indexes. Each pixel in $I(x, y)$ consists of magnitude, α , and phase, θ , information represented as $\alpha e^{i\theta}$. Next define a sequence of ROI images as:

$$\{I_1(x, y), I_2(x, y), \dots, I_N(x, y)\} \quad (1)$$

where each image is of the same ROI at a different time. Coherent change detection is then defined as

$$\delta(x, y) = |I_r(x, y) - I_k(x, y)| \quad (2)$$

where $k \neq r$, and $I_r(x, y)$ is the reference image. Each pixel in $\delta(x, y)$ has the magnitude $\sqrt{\alpha_k^2 + \alpha_r^2 - 2\alpha_k\alpha_r \cos(\theta_k - \theta_r)}$. Non-coherent change detection is defined as

$$\Delta(x, y) = |I_r(x, y)| - |I_k(x, y)| \quad (3)$$

where each pixel in the non-coherent change detection image has the magnitude $|\alpha_r| - |\alpha_k|$. The positive magnitudes in $\Delta(x, y)$ are generated by $|\alpha_r|$, which indicates a contribution from $I_r(x, y)$. The negative magnitudes in $\Delta(x, y)$ are generated by $|\alpha_k|$, which indicates a contribution from $I_k(x, y)$. The non-coherent change detection approach can therefore be used to determine the ROI image (i.e. $I_r(x, y)$ or $I_k(x, y)$) that produces the MT signature, back-wall shadow, front-wall response, and sidelobe imaging artifacts generated in $\Delta(x, y)$.

III. PROPOSED CHANGE DETECTION TECHNIQUE

The processing of the proposed change detection technique is illustrated in Figure 1. This technique determines the MT signature for a given reference image, $I_r(x, y)$, by first generating a set of M non-coherent change detection images:

$$\{\Delta_r(1, x, y), \dots, \Delta_r(k, x, y), \dots, \Delta_r(M, x, y)\} \quad (4)$$

where

$$\Delta_r(k, x, y) = |I_r(x, y)| - |I_{\gamma_k}(x, y)| \quad (5)$$

and $M \leq N$, $1 \leq \gamma_k \leq N$ for a given k , $1 \leq r \leq N$, $\gamma_k \neq r$. Note the following: Equation 4 considers M of N ROI images; $I_r(x, y)$ is constant for all k ; r is the index indicating the reference image; and the parameter γ_k is the index for an ROI image and is dependent upon k . The choices for γ_k and M are application dependent and discussed further in Section IV.

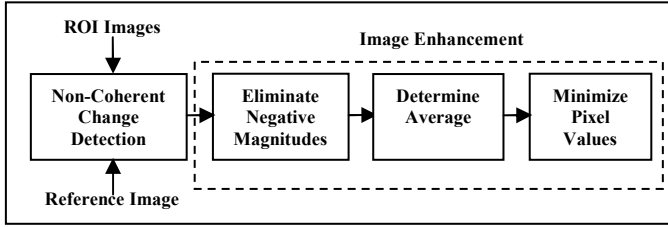


Figure 1: Proposed change detection technique for a given reference image. The proposed technique is based on non-coherent change detection.

Equations 4 and 5 indicate that the MT signature, associated with $I_r(x, y)$, is positive in magnitude and constant in position. In addition, all pixels in image $\Delta_r(k, x, y)$ associated with $I_{\gamma_k}(x, y)$ are negative in magnitude and can be eliminated since these pixels do not contribute to the MT signature of $I_r(x, y)$. Therefore, the second step of the proposed change detection technique is to eliminate the negative magnitudes in each image of Equation 4:

$$\Lambda_r(k, x, y) = \begin{cases} \Delta_r(k, x, y) & \Delta_r(k, x, y) \geq 0 \\ 0 & \Delta_r(k, x, y) < 0 \end{cases} \quad (6)$$

The processing of Equation 6 produces the following sequence of images:

$$\Lambda = \{\Lambda_r(1, x, y), \dots, \Lambda_r(M, x, y)\} \quad (7)$$

The third step of the proposed change detection technique is to average the images in Λ to enhance the MT signature. It is possible that the MT signature is severely attenuated in one or more images in Λ . The minimization process (step 4 in Figure 1) selects the most attenuated MT signature in Λ . Therefore, the severely attenuated MT signature becomes the dominate feature for the minimization process and is characterized as the MT signature for the reference image. In order to prevent a severely attenuated MT signature from being the dominant feature, all MT signatures in Λ are averaged as follows:

$$\Theta_r(i, x, y) = \frac{\Lambda_r(i+1, x, y) + \Lambda_r(i, x, y)}{2} \quad (8)$$

where $1 \leq i \leq M-1$, and produces the following sequence of images:

$$\Theta = \{\Theta_r(1, x, y), \dots, \Theta_r(M-1, x, y)\} \quad (9)$$

Note that, as indicated in (8), the averages described in this work are calculated using two samples. However, the number of samples used to calculate the averages can be increased depending on the application. The final step of the proposed technique is to eliminate sidelobe imaging artifacts using the following minimization procedure:

$$\Psi_r(x, y) = \min_i \{\Theta_r(i, x, y)\} \quad (10)$$

The minimization procedure attenuates sidelobes associated with the MT signature, back-wall shadow, and front-wall response. The minimization procedure is used since the magnitude variations associated with the moving target are less than the magnitude variations associated with the sidelobes [5]. For example, consider the scenario of a person walking cross-range to a radar sensor (from left to right). This scenario has been modeled using near-field scattering simulations (the details of the simulations are discussed in Section IV). ROI images are generated using the back-projection procedure [6] on the simulated data. The proposed change detection technique processes the sequence of ROI images to generate the sequence of images in Θ . The minimization technique (Equation 10) processes the images in Θ and the results are compared, Figure 2, with the results of the maximization technique: $\max_i \{\Theta_r(i, x, y)\}$. The

maximization technique represents the worst case scenario of sidelobe reduction and is compared to the minimization technique to illustrate the significance of sidelobe reduction from the minimization technique. The dynamic range for both images is 50 dB (-95dB to -145dB). A representative pixel of the MT signature and the sidelobe imaging artifacts is chosen to compare power levels between Figures 2-a and 2-b. As is shown, a 4.9 dB difference is observed between the MT signature in Figures 2-a and 2-b. A 29.9 dB difference is observed between the sidelobes of Figure 2-a and those of Figure 2-b. This translates into an increase of approximately 25dB in peak-to-sidelobe ratio. Based on these large power differences, the minimization technique preserves the power associated with the MT signature while greatly attenuating the power associated with the sidelobes.

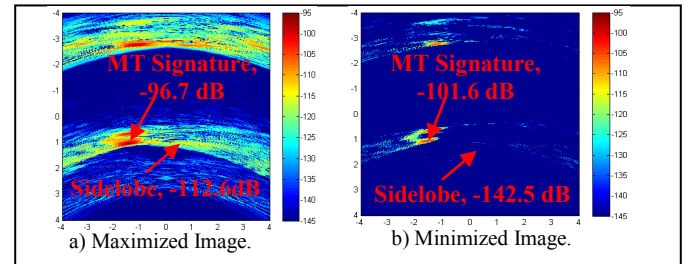


Figure 2: Images generated using a minimization and maximization procedure. A significant difference in sidelobe energy is observed between the images.

$\Psi_r(x, y)$ constitutes the final change detection image generated by the proposed change detection technique for the reference image $I_r(x, y)$. Thus, the MT signature in the reference image is identified and the trajectory of the moving target is determined by changing the reference image index, r . The final set of change detection images are defined as

$$\Psi = \{\Psi_1(x, y), \dots, \Psi_N(x, y)\} \quad (11)$$

IV. SIMULATION RESULTS

The near-field scattering simulations are computed using XPATCH. XPATCH is a physical optics (PO) based code that uses a ray-tracing technique to calculate the scattering field from a target [7]. The simulated radar scattering data are computed for 24 moving target positions shown in Figure 3, where “X” denotes range and “Y” denotes cross-range. The building structure consists of four brick walls and a ground-plane. The walls have a thickness of 8” and are modeled as brick with a dielectric constant of $3.8-j0.24$. The ground-plane has a dielectric constant of 6.8 (dry soil). The antenna array is located 8m from the front wall. The antenna array consists of effectively 17 monostatic antennas distributed across a 2m aperture. For a given antenna position 2404 frequency bins of in-phase and quadrature (I/Q) information is collected. The 2404 frequency bins form the frequency domain representation of an I/Q range profile, and the range profile is constructed via an inverse fast Fourier transform (IFFT). Note that a range profile is generated for each antenna position. The bandwidth of the collected frequency information is 4GHz and ranges from 0.1-4.1GHz.

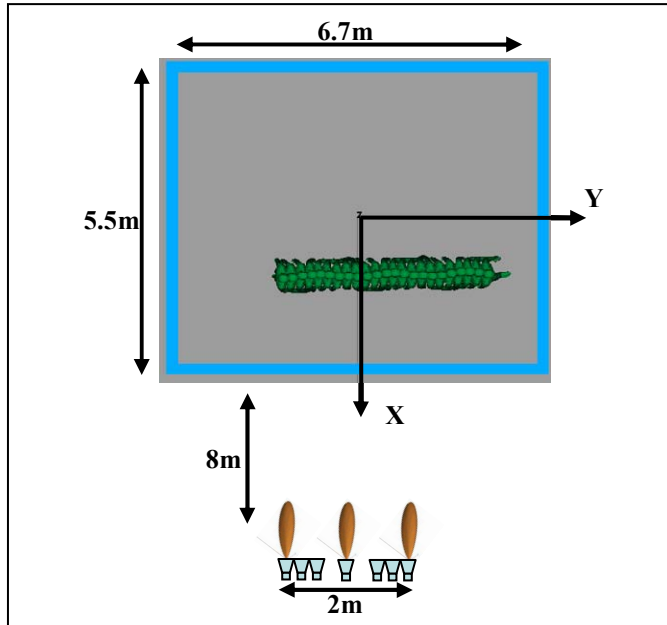


Figure 3: The CAD model of the building structure. 22 moving target positions are simulated.

The 17 I/Q range profiles are collected for each moving target position. For a given moving target position, the 17 I/Q range profiles constitute one frame of data and each frame of data is used to form an ROI image. The moving target

positions are spaced 0.15m apart. The total distance covered by the moving target is 3.6m.

To form an ROI image, each I/Q range profile is first windowed using a Hanning window of size 2404 (i.e. the size of the range profile). The window size is chosen to make the bandwidth of each range profile similar to that of radar measurements (discussed in Section V). The windowed range profile is next converted to a time domain sequence using the IFFT. The time domain sequence is next processed by the back-projection algorithm [6] to focus the raw data. Each ROI image is of size 8x8m and contains 400x400 pixels with a pixel spacing of 0.02x0.02m. 24 ROI images are generated (i.e. $N=24$).

The proposed moving target indication (MTI), non-coherent change detection (MNCD) technique is used to process the $N=24$ ROI images to produce Ψ . $M=8$ non-coherent change detection images are generated where:

$$\{\gamma_1, \dots, \gamma_8\} = \{r-4, r-3, r-2, r-1, r+1, r+2, r+3, r+4\}$$

for $r > 4$ and $r \leq N-4$, where r is the index for the reference image. γ_k is chosen to select the ROI images “closest” to the reference image. The closest ROI images have sidelobe patterns similar to the sidelobe patterns in $I_r(x, y)$. If the distance between the MT signatures of $I_r(x, y)$ and $I_{\gamma_k}(x, y)$ is large, then the sidelobe patterns of the images are unaligned and will not cancel effectively. When $r \leq 4$ and $r > N-4$, i.e. the boundary conditions, γ_k is selected to create a set of ROI images that contains the closest MT signature to the MT signature in $I_r(x, y)$. For example, if $r=3$, then $\{\gamma_1, \dots, \gamma_8\} = \{1, 2, 4, 5, 6, 7, 8, 9\}$.

Three pairs of images are shown in Figure 4. Each pair consists of a change detection image generated by the MNCD technique, i.e. the MNCD image, and by the coherent change detection (CCD) technique (Equation 2), i.e. the CCD image. The images in Figure 4 represent a subset of all the images that were generated and are shown to illustrate key difference between the MNCD and CCD techniques. Each image in Figure 4 is normalized by dividing the magnitude of each pixel by the maximum magnitude of the image. As is shown in Figure 4, the MT signature is clearly visible and identifiable in both the MNCD and CCD images. Figure 5 illustrates a close-up of the MT signature in Figures 4-a and 4-b and reveals that the MT signature generated using the MNCD technique is very similar to the MT signature generated using the CCD technique. If the MT signature generated by the MNCD technique was severely attenuated, then automatic target recognition and tracking results could be adversely affected.

The back-wall shadow, front-wall response, and sidelobe imaging artifacts in the MNCD images of Figure 4 are significantly attenuated compared to those artifacts in the CCD images. To develop a more quantitative understanding of the attenuation, the average power of each artifact category (i.e. sidelobe, shadow, and front-wall) in the MNCD image is estimated and compared to the corresponding average power in the CCD image. The results are illustrated in Figure 4. The

“red box” window in each image indicates the area of pixels that are averaged (note that the window shown in each figure is not drawn to scale). A 24.8 dB attenuation is observed for the sidelobes in the MNCD image using a 1.1×0.4 m (range x cross-range) window. A 21.3 dB attenuation is observed for the back-wall shadow in the MNCD image using a 0.3×0.6 m window. A 14 dB attenuation is observed for the front-wall response in the MNCD image using a 1.3×0.08 m window. The results of this quantitative comparison indicate that the MNCD technique is significantly more effective in attenuating imaging artifacts compared to the CCD technique.

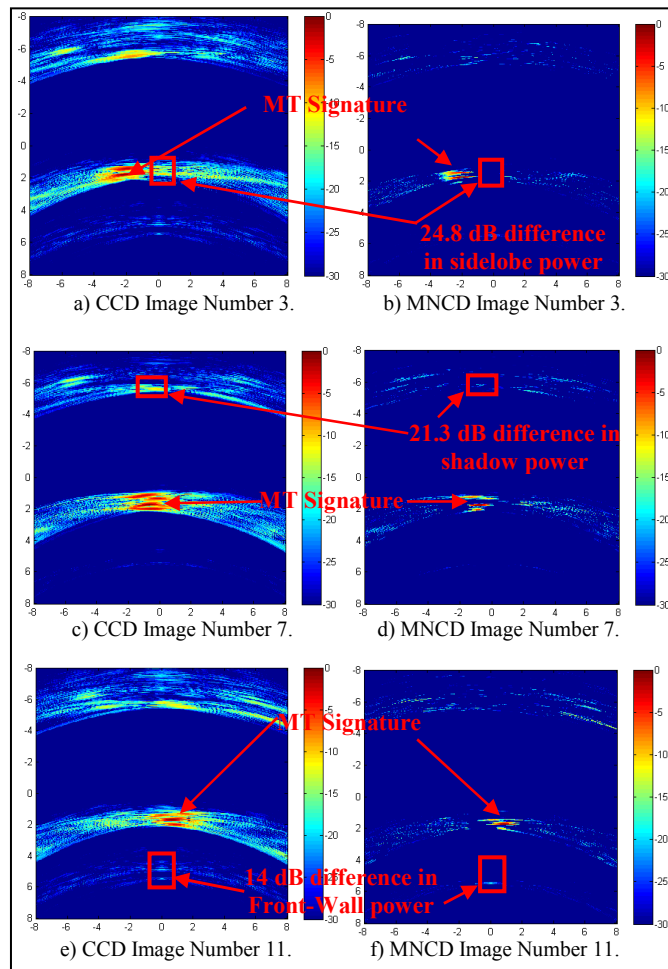


Figure 4: Change detection images of modeled data. Each image is normalized and uses a dynamic range of 30dB. “Image Number” refers to the position of the image in the sequence of all change detection images.

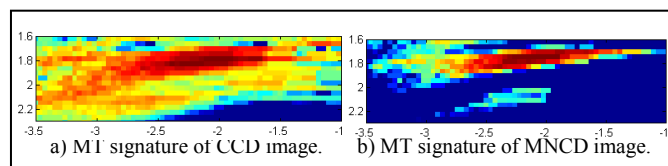


Figure 5: MT signatures of change detection images in Figures 4-a and 4-b. Images are of size 0.7×2.5 m with a 30dB dynamic range.

V. EXPERIMENTAL RESULTS

In addition to processing modeling data, the MNCD and CCD techniques are used to process measurement data collected by the U.S. Army Research Laboratory’s (ARL)

ground-based Synchronous Impulse Reconstruction (SIRE) radar. The SIRE radar is an impulse-based, UWB imaging radar with an effective bandwidth covering 500MHz to 1.5GHz, a frequency range appropriate for sensing through the wall (STTW) applications [1]. As is illustrated in Figure 6, the SIRE radar employs 2 transmit antennas and 16 receiver antennas mounted in a wooden structure and attached to the top of a Ford Expedition. The receive antennas are equally spaced across a linear 2m long aperture. The two impulse transmitters are located at each end of the wooden structure and slightly above the receive array. The SIRE radar constructs a high-resolution (0.15m) down-range profile through ARL-developed signal-processing techniques [6].



Figure 6: The SIRE radar.

For the experiments described in this section, the SIRE radar remains stationary and the downrange swath measured by the radar extends from approximately 8 to 30m. The received measurements are effectively buffered in one downrange profile from each receive channel, and the time required to assemble these profiles represents one frame of data. After buffering the data from one frame, another set of downrange profiles are collected from each receive channel. The down range profiles for each frame are directly processed (without windowing or filtering) using the back-projection algorithm to form a set $N=34$ ROI images. Each ROI image is of size 10×10 m and contains 500×500 pixels with a pixel spacing of 0.02×0.02 m. The ROI images are processed using the CCD and MNCD techniques with the same parameter set described in Section IV.

Two operational scenarios are considered. The first scenario is of a person walking inside a wood building as depicted in Figure 7-a. Two pairs of images are shown in Figure 8. Each pair of images consists of a MNCD image and a CCD image. The images in Figure 8 represent a subset of all the images that were generated and are shown to illustrate key difference between the MNCD and CCD techniques. Each image in Figure 8 is normalized relative to the peak pixel value and has a dynamic range of 20dB. As is shown in Figure 8, the MT signature is clearly visible and identifiable in both the MNCD and CCD images. Closer examination of the MT signature, Figure 9, reveals that the MT signature generated using the MNCD technique is slightly attenuated and remains identifiable. Note also that the MT signature in Figure 9-b (from measurement data) is more attenuated than the MT signature in Figure 5-b (from modeled data) indicating that the fidelity of measurement data is less than that of the model data (as expected).

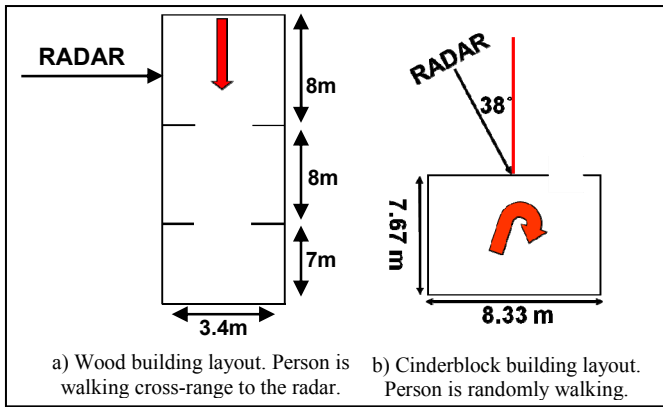


Figure 7: Building layouts for MTI experiments. The red arrows indicate path of the moving target.

The sidelobe, shadow, and front-wall artifacts in the MNCD images of Figure 8 are significantly attenuated compared to those artifacts in the CCD images. Similar to the analysis conducted for the modeling data, the average power of each artifact category in the MNCD image is estimated and compared to the corresponding average power in the CCD image. The results are illustrated in Figure 8. The “red box” window in each image indicates the area of pixels that are averaged. A 16.3 dB attenuation is observed for the sidelobes in the MNCD image using a 1x1m window. A 7.4 dB power attenuation is observed for the back-wall shadow in the MNCD image using a 0.2x1.2m window. A 12.7 dB power attenuation is observed for the front-wall response in the MNCD image using a 0.4x1m window. The results of this comparison indicate that the MNCD technique is significantly more effective in attenuating imaging artifacts compared to the CCD technique.

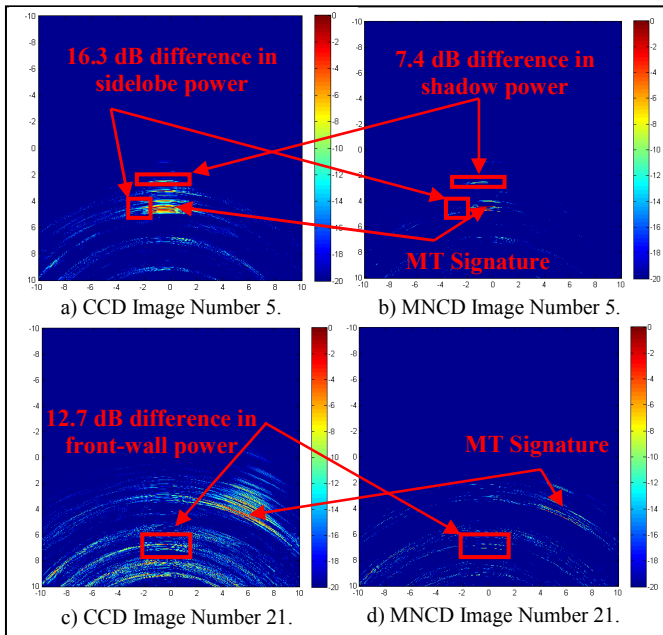


Figure 8: Change detection images of measured data of a wood building. Each image is normalized and uses a dynamic range of 20dB. “Image Number” refers to the position of the image in the sequence of all change detection images.

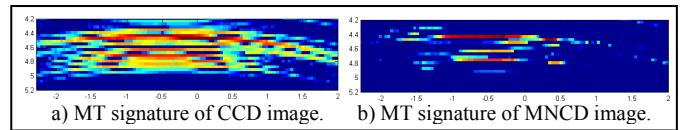


Figure 9: MT signatures of change detection images in Figures 8-a and 8-b. Images are of size 1.0x4.3m with a 20dB dynamic range.

The second operational scenario is of a person randomly walking inside a cinderblock building (Figure 7-b). The radar is position 38° off the broadside position. The off-broadside angle was selected in an attempt to reduce imaging artifacts present in the change detection images due to large reflections from the wall [4]. Two pairs of images are shown in Figure 10. Each pair of images consists of a MNCD image and a CCD image. Each image in Figure 10 is normalized relative to the peak pixel value and has a dynamic range of 20dB. The observations illustrated in Figure 10 (cinderblock building) are similar to those illustrated in Figures 4 (modeled brick building) and 8 (wood building) and are summarized as: 1) the MT signature is clearly visible and identifiable in both the MNCD and CCD images; 2) the MT signature, Figure 11, generated using the MNCD technique is more attenuated compared to the MT signature generated using the CCD technique; 3) the back-wall shadow, front-wall response, and sidelobe imaging artifacts in the MNCD images of Figure 10 are significantly attenuated compared to those artifacts in the CCD images. Power level differences for the artifacts are illustrated in Figure 10. The window sizes used for averaging are as follows: 0.6x1.4m for sidelobe; 0.3x1.4m for shadow; 0.6x1m for front-wall.

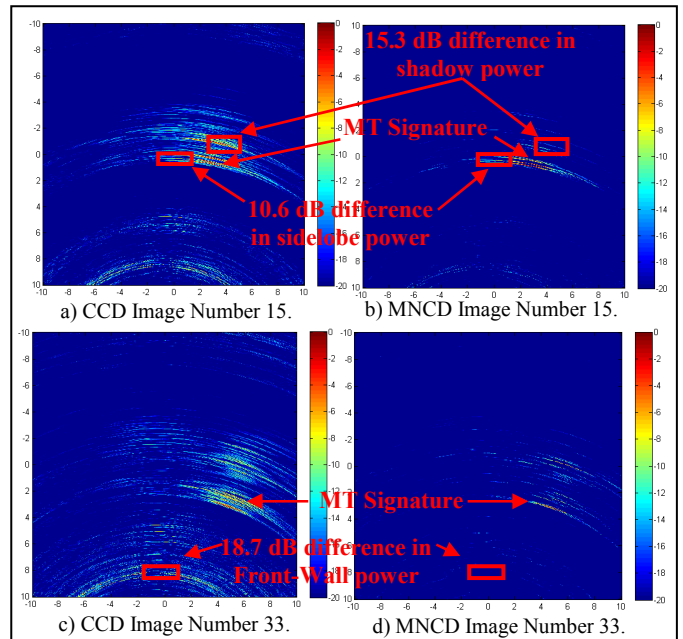


Figure 10: Change detection images of measured data of a cinderblock building. Each image is normalized and uses a dynamic range of 20dB.

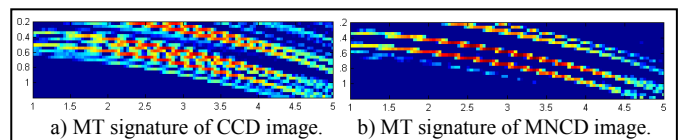


Figure 11: MT signatures of change detection images in Figures 10-a and 10-b. Images are of size 1x4m with a 20dB dynamic range.

Not all imaging artifacts generated using the MNCD technique are significantly attenuated compared to those generated by the CCD technique. For example, consider the cinderblock front-wall response in the CCD and MNCD images of Figure 12. In general the imaging artifacts generated using the MNCD technique appear more attenuated than those generated by the CCD technique, however, this difference is insignificant. In another example, consider the CCD and MNCD images in Figure 13. As is shown significant imaging artifacts are present in the MNCD image and not the CCD image. These imaging artifacts occur when the averaging process (Equation 8) does not properly enhance the MT signature. As discussed in Section III, if the MT signature is severely attenuated then it becomes the dominate feature during the minimization process and is present in the MNCD image. The attenuated MT signature has power similar to imaging artifacts; hence the image in Figure 13-b. The choice for M (i.e. $M=8$) and the number of averages (i.e. two averages) are chosen to prevent attenuated MT signatures and to minimize sidelobe artifacts for the majority of MNCD images. It is verified that the majority of change detection images generated by the MNCD technique contains less imaging artifacts than the set of images generated by the CCD technique.

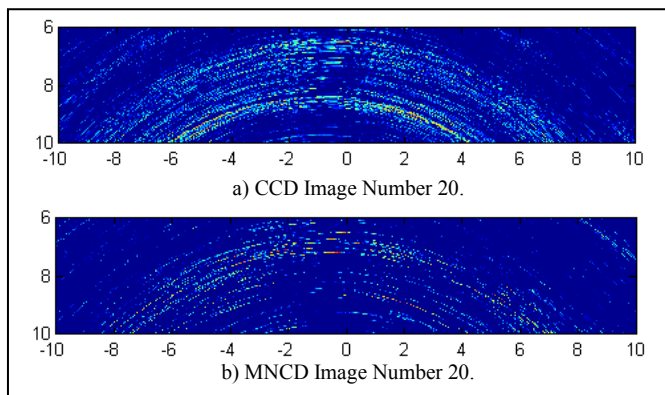


Figure 12: Cinderblock front-wall imaging artifacts of CCD and MNCD images. Images are of size 4x20m with a 20dB dynamic range.

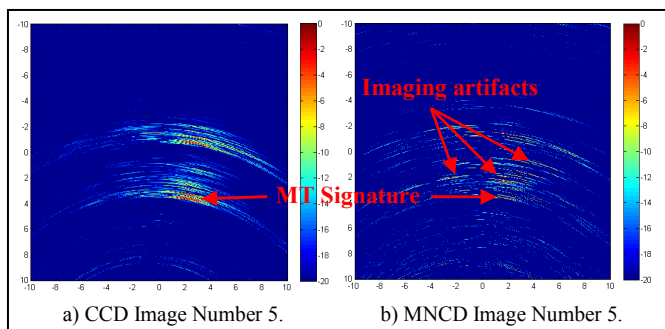


Figure 13: Change detection images of measured data of a cinderblock building. Each image is normalized and uses a dynamic range of 20dB.

VI. SUMMARY

The Moving target indication (MTI) non-coherent change detection (MNCD) technique is a novel and effective method

for identifying the MT signature and eliminating imaging artifacts. The simulation and experimental results demonstrated the effectiveness of the proposed method. In rare cases, the anticipated enhancement of the MNCD image is not realized (see Figure 13). In these cases, imaging artifacts are retained when the averaging process (Equation 8) does not properly enhance the MT signature; the phenomenon is dependent on the number of averages taken and M . As a whole, however, the results indicated a significant attenuation of imaging artifacts observed in the MNCD image relative to those observed in the coherent change detection (CCD) image. The simulation results indicated a 24.8 dB attenuation of the sidelobes, a 21.3 dB attenuation of the shadow, and a 14 dB attenuation of the front-wall response in the MNCD images. The wood building experimental results indicated a 16.3 dB attenuation of the sidelobes, a 7.4 dB attenuation of the shadow, and a 12.7 dB attenuation of the front-wall response in the MNCD images. The cinderblock building experimental results indicated a 10.6 dB attenuation of the sidelobes, a 15.3 dB attenuation of the shadow, and a 18.7 dB attenuation of the front-wall response in the MNCD images.

Based on the parameters chosen for the simulations and experiments presented in this paper, the majority of change detection images generated by the MNCD technique contain less imaging artifacts than those generated by the CCD technique. In future work, the MNCD technique will continue to be evaluated. CFAR and morphological algorithms will be used to process the change detection images generated by the MNCD algorithms to determine P_d and P_{fa} for multiple scenarios.

REFERENCES

- [1] M. Farwell, J. Ross, R. Luttrell, D. Cohen, W. Chin, and T. Dogaru, "Sense through the wall system development and design considerations," *Journal of the Franklin Institute*, vol. 345, no. 6, September 2008, pp. 570-591.
- [2] L. Novak, "Change detection for multi-polarization, multi-pass SAR," in *Proceedings of the SPIE Conference on Algorithms for Synthetic Aperture Radar Imagery XII*, vol. 5808, Orlando, FL, March 2005, pp. 234-246.
- [3] A. Martone, K. Ranney, R. Innocenti, "Through the wall detection of slow moving personnel," in *Proceedings of the SPIE conference on Radar Sensor Technology XIII*, vol. 7308, Orlando, FL, April 2009.
- [4] A. Martone, K. Ranney, R. Innocenti, "Automatic Through the Wall Detection of Moving Targets using Low-Frequency Ultra-Wideband Radar," in *Proceedings of the IEEE International radar conference*, Washington, DC, May 2010.
- [5] L. Nguyen, "SAR imaging technique for reduction of sidelobes and noise," in *Proceedings of SPIE*, vol. 7308, 2009.
- [6] J. McCorkle, "Focusing of Synthetic Aperture Ultra Wideband Data," in *Proceedings of the IEEE International Conference on Systems Engineering*, Dayton, Oh, August 1991, pp. 1-5.
- [7] T. Dogaru, L. Nguyen, C. Le, "Computer Models of the Human Body Signature for Sensing Through the Wall Radar Applications," ARL-TR-4290, U.S. Army Research Laboratory: Adelphi, MD, Sept 2007.